Texture Development of α-Al$_2$O$_3$ Ceramic Coatings by Aerosol Deposition

Makoto Hasegawa[1,*1], Kota Akiyama[1,*2], Yosuke Oki[1,*2], Makoto Tanaka[2], Satoshi Kitaoka[2]
and Yutaka Kagawa[3]

[1]*Division of Materials Science and Chemical Engineering, Faculty of Engineering, Yokohama National University, Yokohama 240–8501, Japan*
[2]*Japan Fine Ceramics Center, Nagoya 456–8587, Japan*
[3]*Research Center for Advanced Science and Technology, The University of Tokyo, Tokyo 153–8904, Japan*

X-ray diffraction and electron backscattering diffraction analyses of the surfaces of α-Al$_2$O$_3$ coatings formed by aerosol deposition and heat treatment up to 1573 K reveal that the coatings have textures. A texture with the (0001) plane inclined approximately 15° away from the coating plane is observed in an as-deposited specimen. During heat treatment, the (0001) plane becomes almost parallel to the coating plane. Texture development is observed with increasing heat treatment temperature. [doi:10.2320/matertrans.M2016213]

1. Introduction

Aerosol deposition (AD), sometimes called aerosol gas deposition or aerosol-type jet printing, is a coating process that can produce dense ceramic coatings by impacting solid particles onto a substrate at room temperature under low-pressure conditions. The basic AD method was developed in the 1980s by Hayashi[1]. The method has received additional attention and undergone development because it is an attractive method of forming dense ceramic coatings[2,3]. Many ceramic powders, such as ZrO$_2$[4–6], α-Al$_2$O$_3$[2,3,7–9], Pb(Zr$_{52}$,Ti$_{48}$)O$_3$[3,10], Ni-Zn-Fe$_3$O$_4$[3], Li$_4$Ti$_5$O$_{12}$[11], AlN[3], MgB$_2$[3], and Ti$_3$SiC$_2$[12] can be deposited to form coatings. It has been reported that the coatings consist of a dense microstructure of small grains with a random orientation distribution[2]. The ability to form coatings up to several micrometers thick without any heating is one advantage of the AD method. These coatings are considered to be fabricated by fracture and/or plastic deformation of the particles. The coating phenomenon is called room-temperature impact consolidation[2,10].

Generally, when plastic deformation occurs in bulk metals or ceramics, a texture forms mainly by the activation of several slip and/or twin systems[13–20]. For bulk Al$_2$O$_3$, it has reported that a (0001) fiber texture forms under hot-pressing and forging at 2073 K[18]. A basal texture develops with increasing strain under compression at 1732 K[19]. The formation of basal texture is indicated by the activation of the basal slip system, grain boundary sliding, and recrystallization under high-temperature compression[18–20]. Thus, when plastic deformation of the Al$_2$O$_3$ particles occurs at room temperature due to impact on the substrate during the AD method, a textured coating can sometimes be obtained. However, texture formation by the AD method has not been sufficiently investigated. Fuchita *et al.* merely indicated the possibility of texture formation after observing differences between the X-ray diffraction pattern for a ZrO$_2$ coating and ZrO$_2$ powder[6]. However, for Al$_2$O$_3$ coatings, it has been reported that

no texture was observed when the orientation distribution was evaluated from a cross section of the coating by selected area electron diffraction during transmission electron microscopy (TEM)[2].

Because it can be used to form dense ceramic coatings at room temperature, the AD method is a candidate process for high-temperature applications. Such dense coatings tend not to shrink during sintering at high temperatures. Thus, they may resist vertical crack initiation by tensile stresses parallel to the interface. Recently, advanced environmental barrier coatings (EBCs) based on a periodic layered structure of Y$_2$Ti$_2$O$_7$ and Al$_2$O$_3$ have been proposed that effectively reflect thermal radiation energy in addition to preventing oxidation of the underlying SiC fiber reinforced SiC ceramic matrix composites (CMCs)[21]. Such EBCs could be formed on CMCs with a bond coat of mullite using the AD method. Thus, the AD method is a promising process for forming protective coatings for severe environments. However, the detailed microstructures of these coatings at high temperatures are not yet known. In this study, the orientation distribution of Al$_2$O$_3$ coatings was investigated using the AD method. α-Al$_2$O$_3$ particles were used because several slip and twin systems are already known[22]. Furthermore, changes in the microstructure and texture during heat treatment were also evaluated experimentally.

2. Experimental Procedure

2.1 Materials

Commercially available α-Al$_2$O$_3$ powder (TM-DAR, Taimei Chemicals Co. Ltd, Nagano, Japan) was used as the starting material. The purity of the powder was 99.99 mass% (impurities: Si 3, Fe 3, Na 3, K 1 Ca 2 Mg 1 ppm), and the average diameter was 140 nm. To dry the powder before deposition, it was heat-treated in air at 523 K for 12 h. Then, the powder was placed in an aerosol container. The AD method was applied at room temperature by blowing the powder from a nozzle (Type GD-AE04/SS2 and/or Type GD-AE24/FC, Fuchita Nanotechnology, Ltd. Tukuba, Japan). Mullite and Y$_2$Ti$_2$O$_7$ were used as substrates, because they are component

---

*1Corresponding author, E-mail: hasegawa@ynu.ac.jp
*2Graduate Student, Yokohama National University

materials for advanced EBCs[21]. Commercial mullite powder (KM101, KCM Co., Ltd., Nagoya, Japan) and Y$_2$Ti$_2$O$_7$ powder, synthesized by spray pyrolysis of an aqueous solution containing Al(NO$_3$)$_3$, Y(NO$_3$)$_3$, and TiCl$_4$, were molded in a uniaxial press at 20 MPa, and then subjected to cold isostatic pressing at 250 MPa. The mullite green compacts were two-step sintered in air at 1573 K for 50 h, followed by 2023 K for 5 h. The Y$_2$Ti$_2$O$_7$ green compacts were sintered in air at 1973 K for 5 h. The relative densities of the sintered samples were over 99% of the corresponding theoretical densities. Disc-shaped substrates were cut from the sintered samples and polished to a mirror-like finish. The dimensions of the mullite and Y$_2$Ti$_2$O$_7$ substrates were Φ15 mm $\times$ 3 mm and Φ23.5 mm $\times$ 0.25 mm, respectively.

During the AD coating process, the N$_2$ gas flow, the pressure inside the coating chamber, and the velocity of the particles measured using the "time-of-flight registration" method[23] were 6 L/min, ~150 Pa, and ~100 m/s, respectively. Two different coating conditions (types A and B) were used. The distance between the nozzle and substrate, the angle of the flow direction from the nozzle to the substrate plane, and the scanning speed of the substrate were 7 mm, 60°, and 50 mm/min for type A and 5 mm, 90°, and 300 mm/min for type B, respectively. After deposition, the specimens were heat-treated from 1173 K to 1673 K for 100 h.

2.2 Microstructural characterization and texture measurement

Cross sections of the specimens were observed by TEM (JEM-2100F, JEOL Ltd., Tokyo, Japan) in order to understand the microstructure change in thickness direction. Electron backscatter diffraction (EBSD) measurements (JSM-7001F, JEOL Ltd., Tokyo, Japan) of the coating surface were performed (OIM Analysis Version 6.2, EDAX Inc., NJ, USA) to make clear the shape and orientation of each crystal grain on the coating. Here, the acceleration voltage was 7 kV and the spot size seems to be ~10 nm. Measurements were conducted at intervals of 50 nm where the scanned area is 18 μm $\times$ 8.3 μm. The minimum rotation angle, θ, between neighboring measured points was calculated. When the θ was larger than 15°, the boundary between the neighboring points was defined as a high angle grain boundary. Textures were measured on the coating plane using the Schulz reflection method with Cu-Kα radiation filtered with a monochromator (Ultima IV, Rigaku Co., Tokyo, Japan). To prevent the overlap of the diffraction peaks from Al$_2$O$_3$ and the substrate, an Y$_2$Ti$_2$O$_7$ substrate was used for the measurements. The $10\bar{1}2$, $11\bar{2}3$, and $11\bar{2}6$ diffracted X-ray intensities were measured for Al$_2$O$_3$ with a rhombohedral lattice. On the basis of the obtained pole figures, the orientation distribution function (ODF) was calculated using the arbitrarily defined cell (ADC) method[24] (LaboTex Version 3.0.24, LaboSoft s. c., Krakow, Poland). The main component and sharpness of the texture, which correspond to the position and value of the maximum pole density, were determined from the normalized pole figure and the inverse pole figure derived from the ODF. The normalized pole density, P(α, β), can be expressed as

$$P(\alpha,\beta) = \frac{I(\alpha,\beta)}{\frac{1}{2\pi}\int_{\alpha=0}^{\alpha=\pi/2}\int_{\beta=0}^{\beta=2\pi} I(\alpha,\beta)\sin\alpha d\alpha\, d\beta}, \quad (1)$$

where I(α, β), α, and β are the non-normalized intensity, radial angle, and azimuthal angle, respectively[25]. In the case of the random specimen, P(α, β) will be 1.0 (mean pole density). The volume fractions for the regions aligned within 15° of the main component were calculated.

3. Results

3.1 Change in microstructure during heating

The cross-sectional microstructures of α-Al$_2$O$_3$ coatings on mullite substrates are shown in Fig. 1. All coatings were approximately 200 nm thick. Fine crystal grains are observed in the as-deposited specimen formed under type-A coating conditions (Fig. 1(a)). With increasing heating temperature and time, the crystal grain size of the coating increases (Fig. 1(b)), and after 100 h at 1573 K, the coating consists of one grain in the thickness direction (Fig. 1(c)). It could not be seen the large difference of microstructure in case of the coatings which were processed by type-A and type-B conditions. Further, drastic change in microstructure after the heat treatment of the coatings deposited by type-A and type-B conditions is also not observed.

Figure 2 shows the results of EBSD measurements for a coating formed under type-B conditions. The specimen was heat-treated at 1673 K for 1 h, and subsequent treatment was conducted at 1573 K for 100 h. In the inverse pole figure map (Fig. 2(a)), almost all of the crystal grains in the map are colored red. This means that the (0001) plane of the α-Al$_2$O$_3$ is almost parallel to the coating surface. Figures 2(b) and 2(c) show (0001) and $\{10\bar{1}0\}$ pole figures, respectively. The pole densities are projected onto the coating plane, and the mean pole density is used as a unit. The pole density distributions form concentric circles, indicating the formation of a fiber texture. In the (0001) pole figure, the position of the maximum pole density is at the center of the pole figure. The pole density is distributed at the great circle in the $\{10\bar{1}0\}$ pole figure. Inverse pole figures showing the pole density distributions in the normal direction (ND) and transverse direction (TD) of the coating plane are shown in Figs. 2(d) and 2(e). The mean pole density is used as a unit. In the ND inverse pole figure, it can be seen that the maximum pole density occurs at the (0001) plane. The maximum pole density is approximately 25 times higher than the random level. In the TD inverse pole figure, the region of high pole density spreads from the $(0\bar{1}10)$ to the $(1\bar{1}00)$ plane. In this case, the maximum pole density is between 2 and 4. Therefore, it seems that
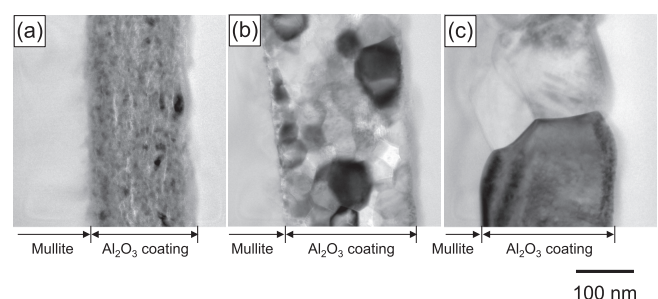

Fig. 1 Transmission electron micrographs of Al$_2$O$_3$ coatings. (a) As-deposited, and heat-treated at (b) 1273 K for 5 h and (c) 1573 K for 100 h.

the presence of a developed texture can be detected from the ND direction, but not the TD direction. However, this analysis was based on the EBSD measurements, which were limited because they only examined a small region. If the coating has a heterogenous microstructure, it has a possibility to have a different orientation distribution in different region. Further, it is technically difficult to detect the EBSD pattern in case of the as-deposited coating due to the small crystal grain size. Only the crystal orientation at the surface region of the coating could be detected as for EBSD measurement, it could not evaluate the average crystal orientation distribution in whole coating thickness as the XRD could analyze the average crystal orientation distribution in 200 nm thick layer. In order to determine the characteristics of entire coatings, the textures were investigated using XRD.

3.2 Texture

Figure 3 shows the texture derived from XRD. An Al_2O_3 coating was processed under type-A conditions (as-deposited state). Figures 3(a) and 3(b) show (0001) and {$10\bar{1}0$} pole figures, respectively, with the pole densities projected onto the coating plane. Figures 3(c) and 3(d) show inverse pole figures from the ND and TD directions of the coating plane, respectively. The mean pole density is used as a unit. These pole figures show that the coating has a fiber texture. In the (0001) pole figure, the maximum pole density spreads approximately 15° away from the center. In the {$10\bar{1}0$} pole figure, the pole density is distributed roughly 15° away from the great circle. Figure 3(c) shows an inverse pole figure from the ND direction. It can be seen that the maximum pole density is oriented approximately 15° away from the (0001) plane. The maximum pole density is 3.5 times higher than the random level. In the inverse pole figure from the TD direction, the region of high pole density spreads from the ($2\bar{1}\bar{1}0$) to the ($11\bar{2}0$) plane. In this case, the maximum pole density is only about 1.5. These results indicate that in order to determine the correct distribution of the orientation, texture analysis based on ODF calculations is required. When the orientation distribution of the coating is analyzed only from the side direction by TEM electron diffraction, in this case, it could be evaluated as random, even if it has a texture from the ND direction. Figure 4 shows the development of texture with increasing heat treatment temperature. Figures 4(a)–(c) show inverse pole figures for Al_2O_3 coatings from the ND direction after heating at dif-
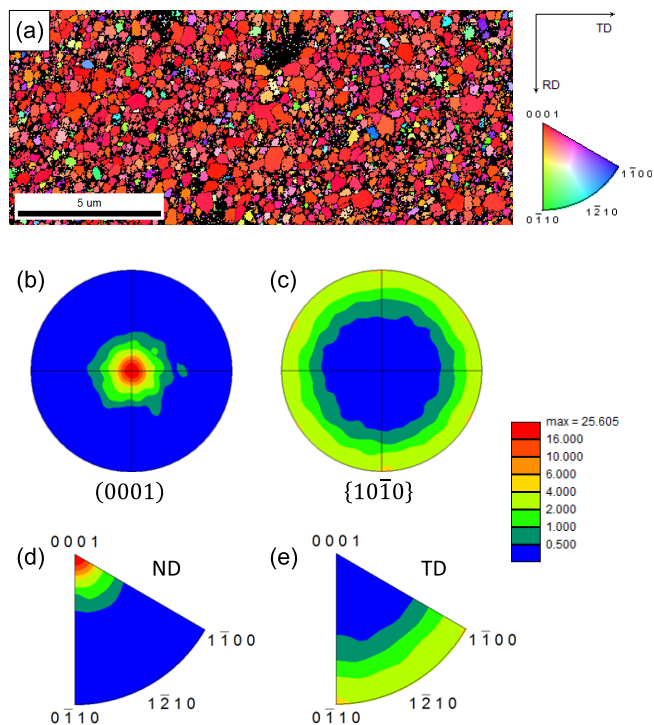

Fig. 2   Orientation distribution analysis of Al_2O_3 coatings using EBSD. (a) Inverse pole figure map, in which the color on the map follows the stereographic triangle. (b) (0001) pole figure, (c) {$10\bar{1}0$} pole figure, (d) inverse pole figure from the ND direction of the coating surface and (e) inverse pole figure from the TD direction.
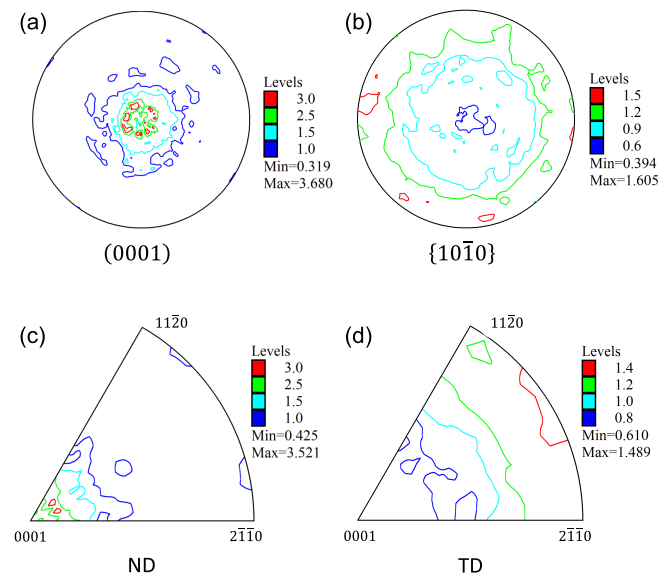

Fig. 3   Orientation distribution of an as-deposited Al_2O_3 coating. (a) (0001) pole figure, (b) {$10\bar{1}0$} pole figure, (c) inverse pole figure from the ND direction and (d) inverse pole figure from the TD direction.
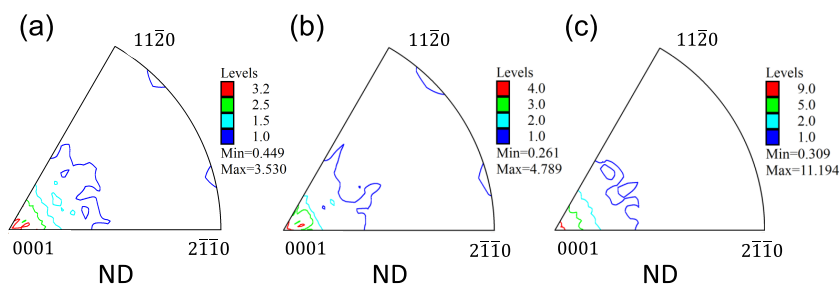

Fig. 4   Inverse pole figures from the ND direction after heat treatment. Heat-treated for 5 h at (a) 1173 K, (b) 1273 K, and (c) 1573 K.
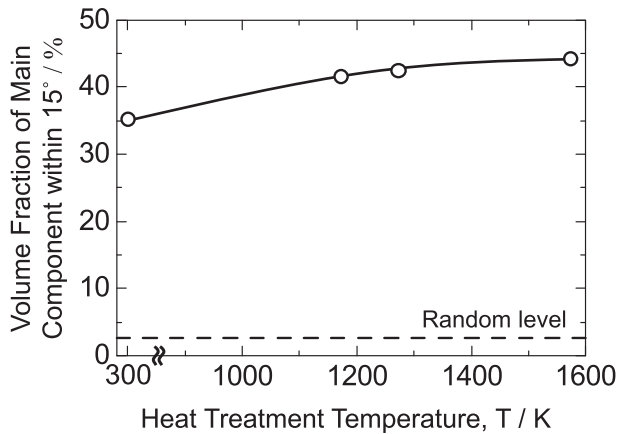
Fig. 5 Relationship between the volume fraction of main component and the heat treatment temperature.

Fig. 6 Standard (0001) projection of α-Al$_2$O$_3$ showing slip planes (filled circles) and slip directions (open circles). Gray region is the standard unit stereographic triangle for α-Al$_2$O$_3$ system.

ferent temperatures for 5 h. The main component changes from that for the as-deposited specimen, is located in the (0001) plane, and has a fiber texture. The maximum pole density increases with increasing heat treatment temperature. The change in the volume fraction of the main component is shown in Fig. 5. Similar to the maximum pole density, the volume fraction increases with increasing heat treatment temperature.

4. Discussion

4.1 Texture formation during AD coating

It has been proposed that the mechanism of AD coating occurs through room-temperature impact consolidation, which involves fracture and/or plastic deformation of the particles during deposition[2,10]. However, the compressive strain rate for Al$_2$O$_3$ particles at impact consolidation during the AD process cannot be determined accurately. Furthermore, there is no information regarding which type of fracture and/or plastic deformation will be active during the AD process.

Two types of deformation behavior and subsequent cracking were observed for different strain rates in bulk Al$_2$O$_3$[26,27]. Deformation involving multiple slip and occasional twinning has been detected over a wide range of compressive strain rates from 10^{-4} to 10^6 s^{-1}. In this case, mechanical tests were performed by indentation, servo-controlled hydraulic testing, split Hopkinson pressure bar (SHPB) testing and a flyer plate experiment, for which the strain rates were 3.5×10^{-3} s^{-1}, 10^{-4}–10^0 s^{-1}, 500–2500 s^{-1}, and 10^5–10^6 s^{-1}, respectively[26]. Under indentation deformation, basal slip, non-basal slip (prism slip and pyramidal slip), basal twinning and rhombohedral twinning have been reported for sapphire single crystals[28,29]. Basal slip, basal twinning, and slip along the (0001) plane having a Burgers vector with $\langle 10\bar{1}0 \rangle$ direction have been observed under shock loading at room temperature in sapphire[30]. Further, transgranular fracture, intergranular fracture, basal slip, prism slip, and twinning have been observed during experimental impact compression of polycrystalline Al$_2$O$_3$[31]. In α-Al$_2$O$_3$ particles, extensive slip with a high dislocation density (10^{11} cm^{-2}) has been observed under explosive shock loading[32]. In all cases, nearly the same fracture, slip, and twining phenomena occur for a wide range of
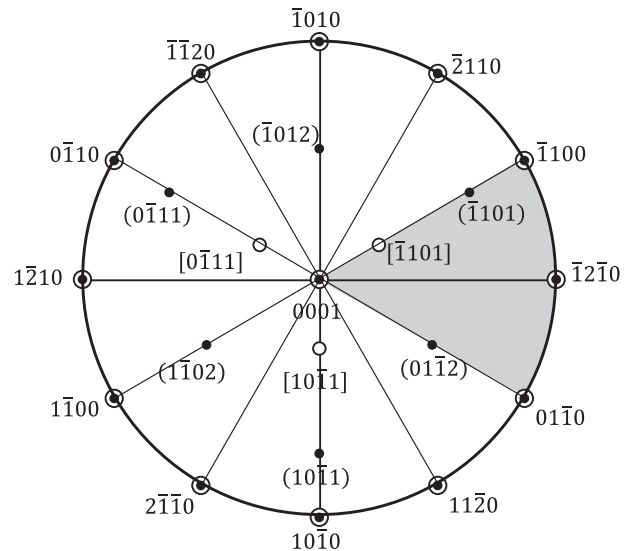
strain rates. Thus, it can be assumed that several types of fracture and plastic deformation take place during the AD process.

If we assume intergranular fracture of the Al$_2$O$_3$, the coating would have no preferential orientation because the fractured grains would be spread randomly. As for transgranular fracture, we must consider which planes will break most easily. It is known that the fracture energy for the (0001) plane (> 40 J/m^2) is about 6 times those of the $\{10\bar{1}0\}$ plane (7.3 J/m^2) and the $\{10\bar{1}2\}$ plane (6.0 J/m^2)[33]. Therefore, transgranular fracture occurs mainly along the $\{10\bar{1}0\}$ and/or $\{10\bar{1}2\}$ planes, rather than the (0001) plane. Thus, when particle fracture occurs mainly on the same planes in collisions with the substrate, the $\{10\bar{1}0\}$ and/or $\{10\bar{1}2\}$ planes will be parallel to the coating plane, due to stacking of the fractured planes. However, the textures will be completely different from what we have observed. Thus, in the present coating process, the coatings are probably formed mainly by plastic deformation of the particles.

Several kinds of slip systems such as (0001)$\langle 11\bar{2}0 \rangle$ (basal slip), $\{11\bar{2}0\}\langle 1\bar{1}00 \rangle$ (prism slip), and $\{10\bar{1}1\}\langle \bar{1}101 \rangle$ (pyramidal slip), and twin systems such as (0001)$\langle 01\bar{1}0 \rangle$ (basal twin) and $\{01\bar{1}2\}\langle \bar{1}01\bar{1} \rangle$ (rhombohedral twin) have been reported for Al$_2$O$_3$[22]. The temperature dependence of the shear stress for the initial yield by slip and twinning, which relates to the critical resolved shear stress (CRSS) in Al$_2$O$_3$, has been estimated by Clayton[22,34]. The shear stress in each slip and twin system decreases with increasing temperature[22,34,35]. The shear stresses at room temperature (300 K) for basal slip, prism slip, pyramidal slip, basal twinning, and rhombohedral twinning are found to be 4.2, 3.2, 6.2, 4.3, and 0.9 GPa, respectively. Rhombohedral twinning has the lowest shear stress, but is activated only under tensile loading[22]. Further, twinning is not observed in α-Al$_2$O$_3$ particles[32], and thus, it can be assumed that activation of the slip systems only occurs under compressive loading. Figure 6 shows the standard (0001) projection for α-Al$_2$O$_3$, indicating the slip planes (filled circles) and slip directions (open circles)[36]. From the

positions of the Al atoms at the available cation sites, it is clear that the *c*-axis has only 3-fold rotational symmetry. Thus, the gray region shown in the standard (0001) projection is presumably the standard unit stereographic triangle for α-Al$_2$O$_3$. In this stereographic triangle, four slip systems, e.g., (0001)[$\bar{1}2\bar{1}0$], ($\bar{1}2\bar{1}0$)[$\bar{1}010$], ($\bar{1}2\bar{1}0$)[$10\bar{1}0$], and ($\bar{1}101$)[$10\bar{1}1$], are the main slip systems. It is generally known that the slip plane is activated to become parallel to the compression plane when the material is compressed[37].

In the AD process, compressive deformation of Al$_2$O$_3$ particles occurs at room temperature. In terms of the shear stress value, prism slip should be the most active slip system. However, in this case, the activation of prism slip may incline the {11$\bar{2}$0} plane parallel to the compression plane. This slip system cannot develop the texture that we have detected. It could possibly activate several slip systems synchronously. The shear stresses associated with prism slip and pyramidal slip at room temperature are 0.8 and 1.5 times higher than that for basal slip. At high temperature (e.g., at 1723 K) where a (0001) fiber texture has formed for bulk Al$_2$O$_3$, the shear stresses for basal slip, prism slip, and pyramidal slip are 23, 104, and 644 MPa, respectively[22]. In this case, the shear stresses for prism slip and pyramidal slip are, respectively, 4.5 and 27.6 times higher than that for basal slip. Given the large difference between the ratio of the shear stress for basal slip and other slip systems, it is appropriate to consider the formation of basal texture by basal slip under high-temperature forging[18–20]. The shear stress ratio at room temperature is almost the same as that under high-temperature conditions. Therefore, several slip systems can be activated at the same time. Both basal and pyramidal slip systems may be triggered concurrently during the AD process. Activation of basal slip and pyramidal slip may incline the (0001) plane and {10$\bar{1}$1} plane parallel to the compression plane. Thus, owing to the occurrence of cross slips by both slip systems, a texture may form in which the (0001) basal plane is inclined approximately 15° away from the compression plane. Furthermore, it seems that because of the low volume fraction of the texture, intergranular fracture has also occurred. To understand the mechanisms of texture formation in the AD method in greater detail, further research is required.

4.2 Evolution of texture at high temperature

A texture developed and changed into the (0001) fiber texture during heat treatment. Furthermore, the grain size in the Al$_2$O$_3$ coating increased with increasing heat treatment temperature and time. From these results, we can assume that the crystal grains in which (0001) is parallel to the coating plane have grown preferentially during heat treatment. It has been reported that the surface energy for the (0001) plane calculated by an *ab initio* methodology is the lowest for Al$_2$O$_3$[38]. The crystal grains exist at the as-deposited coating surface and/or the grains reaching the coating surface during grain growth under heating in which the (0001) plane is parallel to the coating plane seem to increase preferentially in order to reduce the energy of the coating formed.

5. Concluding Remarks

A fiber texture was developed in α-Al$_2$O$_3$ coatings formed using the aerosol deposition (AD) method. Under the as-deposited condition, the (0001) plane was inclined approximately 15° away from the coating plane. This texture is believed to form by the plastic deformation of Al$_2$O$_3$ particles. After heat treatment, the (0001) plane became parallel to the coating plane, owing to the low surface energy of the (0001) plane. The volume fraction of the (0001) plane increased with increasing heat treatment temperature and time.

REFERENCES

1) C. Hayashi, *Oyo buturi,* 54 (1985) 687–693.
2) J. Akedo: J. Am. Ceram. Soc. **89** (2006) 1834–1839.
3) J. Akedo: J. Thermal Spray Technology **17** (2008) 181–198.
4) E. Fuchita, E. Tokizaki and Y. Sakka: J. Ceram. Soc. Jpn. **118** (2010) 767–770.
5) E. Fuchita, E. Tokizaki, E. Ozawa and Y. Sakka: J. Ceram. Soc. Jpn. **118** (2010) 948–951.
6) E. Fuchita, E. Tokizaki, E. Ozawa and Y. Sakka: J. Ceram. Soc. Jpn. **119** (2011) 271–276.
7) D.-W. Lee, H.-J. Kim, Y.-H. Kim, Y.-H. Yun and S.-M. Nam: J. Am. Ceram. Soc. **94** (2011) 3131–3138.
8) K. Naoe, M. Nishiki and A. Yumoto: J. Thermal Spray Technology **22** (2013) 1267–1274.
9) K. Naoe, K. Sato and M. Nishiki: J. Ceram. Soc. Jpn. **122** (2014) 110–116.
10) J. Akedo and M. Lebedev: Jpn. J. Appl. Phys. **38** (1999) 5397–5401.
11) R. Inada, K. Shibukawa, C. Madada, Y. Nakanishi and Y. Sakurai: J. Power Sources **253** (2014) 181–186.
12) M.A. Piechowiak, J. Henon, O. Durand-Panteix, G. Etchegoyen, V. Coudert, P. Marchet and F. Rossignol: J. Eur. Cera. Soc. **34** (2014) 1063–1072.
13) C.S. Barrett and L.H. Levenson: Trans. AIME **137** (1940) 112–127.
14) U. F. Kocks, C. N. Tome and H-R Wenk, Texture and Anisotropy, Cambridge University Press, Cambridge (1998) 179–281.
15) M. Hasegawa, M. Yamamoto and H. Fukutomi: Acta Mater. **51** (2003) 3939–3950.
16) M. Hasegawa and H. Fukutomi: Mater. Sci. Eng. A **508** (2009) 106–113.
17) H. Fukutomi, Y. Konno, K. Okayasu, M. Hasegawa and H. Nakatsugawa: Mater. Sci. Eng. A **527** (2009) 61–64.
18) Y. Ma and K.J. Bowman: J. Am. Ceram. Soc. **74** (1991) 2941–2944.
19) A.H. Heuer, N.J. Tighe and R.M. Cannon: J. Am. Ceram. Soc. **63** (1980) 53–58.
20) W.H. Rhodes, D.J. Sellers and T. Vasilos: J. Am. Ceram. Soc. **58** (1975) 31–34.
21) M. Tanaka, T. Matsudaira, M. Wada, S. Kitaoka, M. Yoshida, O. Sakurada and Y. Kagawa: J. Soc. Mater. Sci. Jpn. **64** (2015) 431–437.
22) J.D. Clayton: Int. J. Plast. **26** (2010) 1357–1386.
23) M. Lebedev, J. Akedo, K. Mori and T. Eiju: J. Vac. Sci. Technol. A **18** (2000) 563–566.
24) K. Pawlik, J. Pospiech and K. Lüche: Text. Microstruct. **14** (1991) 25–30.
25) U. F. Kocks, C. N. Tome and H-R Wenk, Texture and Anisotropy, Cambridge University Press, Cambridge (1998) 149.
26) J. Lankford, W.W. Predebon, J.M. Staehler, G. Subhash, B.J. Pletka and C.E. Anderson: Mech. Mater. **29** (1998) 205–218.
27) J.M. Staehler, W.W. Predebon, B.J. Pletka and G. Subhash: Mater. Sci. Eng. A **291** (2000) 37–45.

28) B.J. Hockey: J. Am. Ceram. Soc. **54** (1971) 223–231.
29) H.M. Chan and B.R. Lawn: J. Am. Ceram. Soc. **71** (1988) 29–35.
30) Y. Wang and D.E. Mikkola: J. Am. Ceram. Soc. **75** (1992) 3252–3256.
31) N.K. Bourne, J.C.F. Millett, M. Chen, J.W. McCauley and D.P. Dandekar: J. Appl. Phys. **102** (2007) 073514.
32) E.K. Beauchamp, M.J. Carr and R.A. Graham: J. Am. Ceram. Soc. **68** (1985) 696–699.
33) S.M. Wiederhorn: J. Am. Ceram. Soc. **52** (1969) 485–491.
34) J.D. Clayton: Proc. R. Soc. Lond. A **465** (2009) 307–334.
35) K.P.D. Lagerlöf, A.H. Heuer, J. Castaing, J.P. Riviére and T.E. Mitchell: J. Am. Ceram. Soc. **77** (1994) 385.
36) J.D. Snow and A.H. Heuer: J. Am. Ceram. Soc. **56** (1973) 153–157.
37) W. F. Hosford, Mechanical Behavior of Materials, 2010, Cambridge University Press pp. 123.
38) A. Marmier and S.C. Parker: Phys. Rev. B **69** (2004) 115409.